Silhouette-based 3D Shape Reconstruction of a Small Body from a Spacecraft

Saptarshi Bandyopadhyay
Jet Propulsion Laboratory
California Institute of Technology
4800 Oak Grove Dr,
Pasadena, CA 91109
+1-626-318-4174
Saptarshi.Bandyopadhyay@jpl.nasa.gov

Issa Nesnas
Jet Propulsion Laboratory
California Institute of Technology
4800 Oak Grove Dr,
Pasadena, CA 91109
+1-818-354-9709
Issa.A.Nesnas@jpl.nasa.gov

Shyam Bhaskaran
Jet Propulsion Laboratory
California Institute of Technology
4800 Oak Grove Dr,
Pasadena, CA 91109
+1-818-354-3152
Shyamkumar.Bhaskaran@jpl.nasa.gov

Benjamin Hockman
Jet Propulsion Laboratory
California Institute of Technology
4800 Oak Grove Dr,
Pasadena, CA 91109
+1-626-639-5505
benjamin.j.hockman@jpl.nasa.gov

Benjamin Morrell
Jet Propulsion Laboratory
California Institute of Technology
4800 Oak Grove Dr,
Pasadena, CA 91109
+1-646-853-9154
benjamin.morrell@jpl.nasa.gov

Abstract— **In this paper, we present a novel Shape from Silhouette (SfS) algorithm to estimate the physical and dynamical properties of a small body—such as an asteroid or comet—from periodic images taken from a distant approaching spacecraft. Standard mapping techniques such as Stereo-Photo-Clinometry (SPC) and Stereo-Photo–Grammetry (SPG) are designed for close-proximity observations in which the body is 1000s of pixels in area, and there are enough surface features on the object. In contrast, our algorithms are suited for distant observations (i.e. during first approach) in which the body is only $10s$–$100s$ of pixels in area and does not present any useful visual features. First, using the Fast-Fourier-Transform of the light curve of the small body, we estimate its rotation rate. Then, using our novel silhouette-based 3D shape reconstruction technique, we estimate the shape and size of the small body and its pole of rotation. In this paper, we assume that the small body is performing pure rotation (no tumbling) about its principal axis, that the Sun is directly behind the spacecraft, and that the distance from the spacecraft to the small body is known. These algorithms have been tested using both simulated data from Comet 67P, Asteroids Eros and Itokawa; and real data from the Rosetta mission.**

TABLE OF CONTENTS

1. INTRODUCTION 1
2. PROBLEM STATEMENT 3
3. ESTIMATING PERIODICITY FROM BRIGHTNESS ... 3
4. ESTIMATING ROTATION CENTER 5
5. ESTIMATING 3D SHAPE USING SILHOUETTE-BASED RECONSTRUCTION 6
6. SHAPE FROM SILHOUETTE (SFS) ALGORITHM 8
7. NUMERICAL SIMULATIONS 9
8. CONCLUSION 9
ACKNOWLEDGMENTS 10
REFERENCES 11
BIOGRAPHY 12

978-1-5386-6854-2/19/$31.00 ©2019 IEEE

1. INTRODUCTION

A number of small body (asteroid, comets) exploration missions have been undertaken to date, such as JAXA's Hayabusa mission to near-Earth asteroid Itokawa launched in May 2003 [1] (see Fig. 1), ESA's Rosetta–Philae mission to Comet 67P which launched in March 2004 [2], [3] (see Fig. 3), NASA's Deep Impact mission to comet Tempel 1 launched in January 2005 [4] (see Fig. 4), and NASA's Dawn mission to asteroids Vesta and Ceres launched in September 2007 [5].

Figure 1. Artist's representation of the Hayabusa spacecraft near asteroid Itokawa. (image credit: JAXA [6])

Moreover, two sample-return missions are currently under way, including JAXA's Hayabusa2 spacecraft which recently deployed three landers to the surface of asteroid 162173

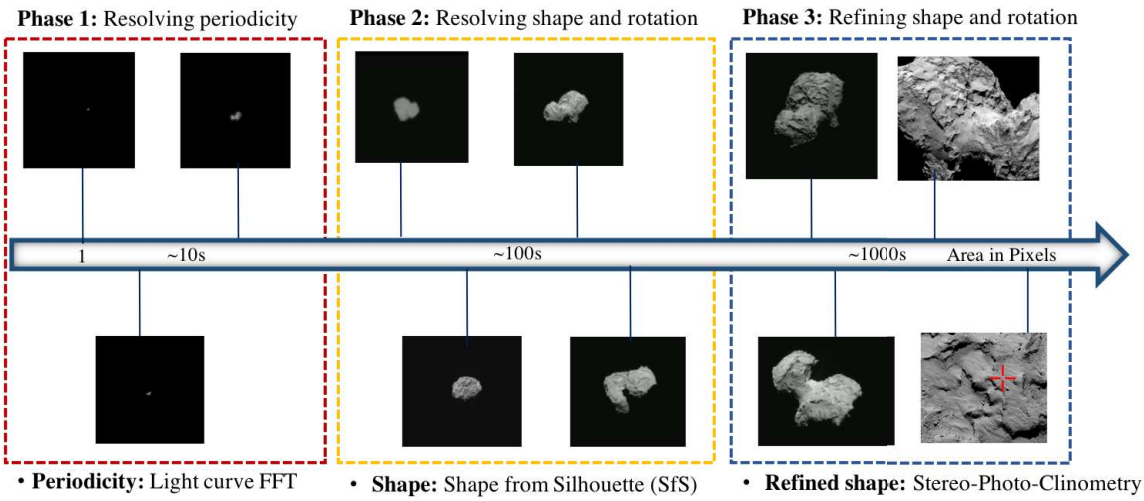

Figure 2. The multi-phased sequence of algorithms to estimate the physical and dynamical parameters of the small body.

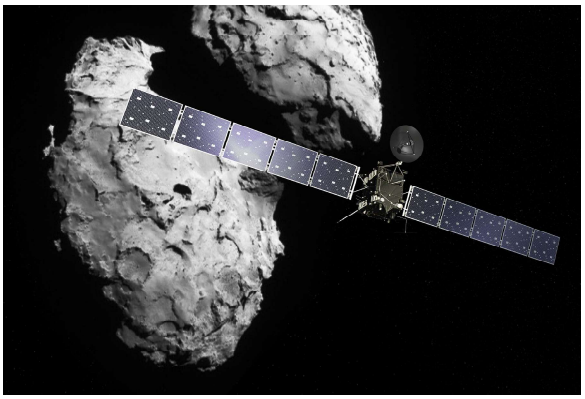

Figure 3. Artist's representation of the Rosetta spacecraft near Comet 67P. (image credit: ESA [7])

Figure 4. Artist's representation of the impactor from Deep Impact striking the comet Tempel 1 while the spacecraft observes the result. (image credit: NASA [8])

Ryugu [9], and NASA's OSIRIS-REx, mission will reach the asteroid 101955 Bennu near the end of 2018 [10]. Future planned missions include NASA's two 2018 Discovery selections, Psyche, which aims to explore a primordial metallic asteroid [11], and Lucy, which will tour several of Jupiter's trojan asteroids [12]

When a spacecraft approaches a small body from a large distance (up to 1000 km), it periodically images the small body to aid spacecraft navigation. The images provide information to estimate the position and attitude of the spacecraft with respect to the small body, as well as estimates of the shape, size, and spin of the small body [13]. A number of algorithms and techniques, like Stereo-Photo-Clinometry (SPC) [14], have been developed to use these images when the small body is 1000s of pixels in area, and there is enough detail to extract surface features on the object. However, these algorithms do not work when images are taken from a very large distance, where the small body is less than 1000 pixels in area and no surface features are discernible.

We claim that there is valuable information in the images even when the small body is only $10s$–$100s$ pixel in size because its silhouette is in sharp contrast against the dark background. Currently, however, there are no algorithms that make use of the information in these images. In this paper, we present a novel Shape from Silhouette (SfS) algorithm to perform silhouette-based 3D shape reconstruction of the small body based on these images. Fig. 2 shows the multi-phased system approach that we developed to estimate the physical (size and shape) and dynamical (rotation rate and pole) parameters of an unknown small body. During Phase 1, where the body is less than tens of pixels in area, we estimate the body's periodicity (magnitude of angular rotation) from variations in pixel intensities (light curves). In Phase 2, where the body is ten to a hundred pixels in area, we use the strong signature of the body's silhouette to resolve its initial shape and rotation axis, given estimates of periodicity from Phase 1. During Phase 2, the images do not adequately resolve surface features for image-based matching techniques like SPC. In Phase 3, as the spacecraft continues to approach the small body, surface features get more resolved, and the body's projection in the camera images grows in pixels. During this phase, we use SPC algorithms, which are seeded by body shape and rotation estimates from Phase 2, to refine the geometry and rotation by matching visual surface features in subsequent frames. The information from each phase is also used to refine the spacecraft's trajectory.

In this paper, we focus on the algorithms for Phase 1 and Phase 2, because the algorithms for Phase 3 are mature and widely used in practice. This paper is organized as

follows: The problem statement for estimating the physical and dynamical parameters of the small body and important assumptions used throughout the paper are discussed in Section 2. The periodicity from brightness algorithm used in Phase 1 is presented in Section 3. The building blocks for the SfS algorithm, namely estimating the rotation center and silhouette-based 3D shape reconstruction are presented in Sections 4 and 5 respectively. The SfS algorithm used in Phase 2 is presented in Section 6. Numerical simulations on the robustness and sensitivity of the algorithms are presented in Section 7. This paper is concluded in Section 8.

2. Problem Statement

Our objective is to estimate the physical (size and shape) and dynamical (rotation rate and pole) parameters of the small body using only the light curve and silhouette information in the images, where the small body is less than 1000 pixels in area. In this paper, we adopt the following assumptions.

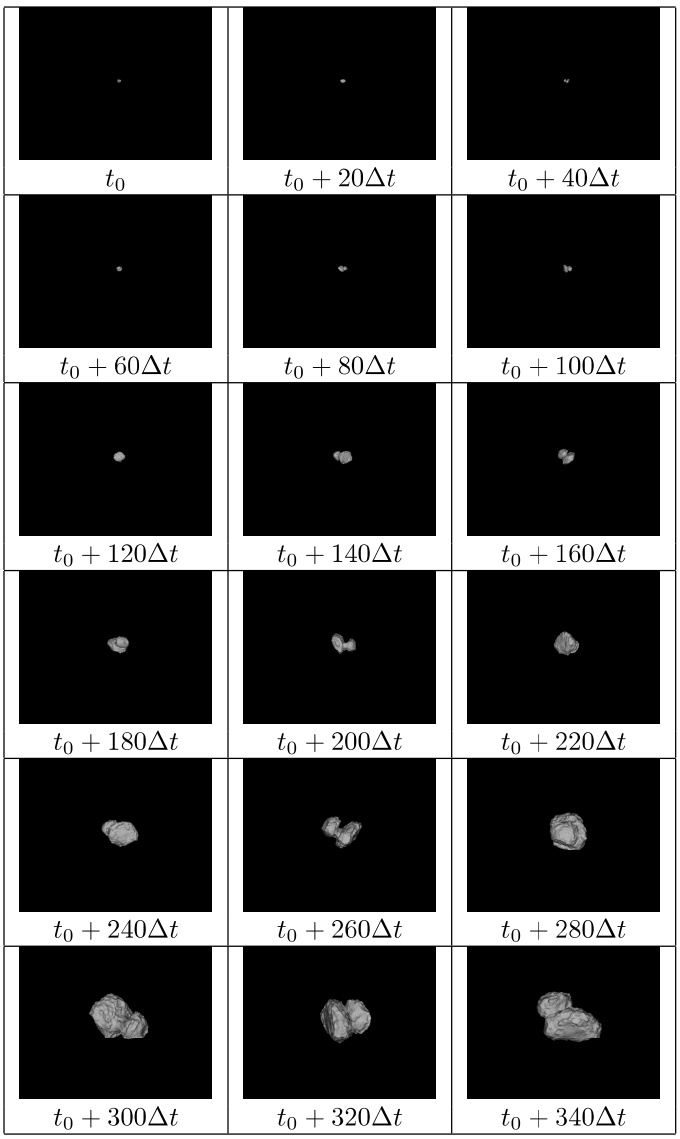

Figure 5. Simulated images of Comet 67P from the Rosetta spacecraft. Here $t_0 = 31^{\text{st}}$ July 2014, 10AM and $\Delta t = 30$ mins.

Assumption 1: We assume that the small body is performing pure rotation (no tumbling) about its principal axis in order to simplify the estimation process. This is a good assumption since a vast majority of small bodies encountered in space to date have exhibited pure rotation. Moreover, it is well-known that a spinning, tumbling body in an energy-dissipative medium converges to spinning about its principle axis [15]. Some slowly rotating asteroid might be in non-principal axis rotations or chaotic tumbling rotation due to Yarkovsky–O'Keefe–Radzievskii–Paddack effect [16].

Assumption 2: We assume that the Sun is directly behind the spacecraft and fully illuminating the small body. We use this assumption to develop the algorithms, but later study the sensitivity of our algorithms to the sun angle in Section 7.

Assumption 3: We assume that the distance from the spacecraft to the small body is known. We use this assumption to develop the algorithms, but removing this assumption will be the main focus of our future research.

Assumption 4: We assume that the orientation of the spacecraft (and hence the camera), with respect to time, is known. This information is routinely collected for all spacecraft.

In this paper, we show that we can estimate the physical and dynamical parameters of the small body under these assumptions.

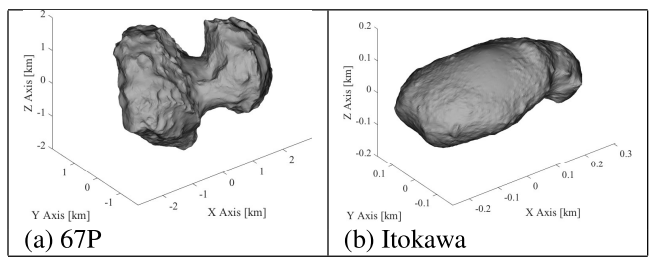

Figure 6. Shape models of Comet 67P and Asteroid Itokawa.

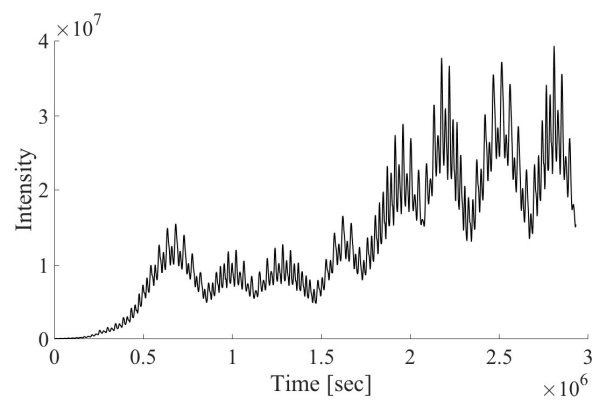

Figure 7. Light curve of Comet 67P with respect to time, obtained from simulated images in Fig. 5

3. Estimating Periodicity from Brightness

As the spacecraft approaches the small body from a large distance, it periodically images the small body as shown in Fig. 5. Here we use the shape model of Comet 67P [17], which rotates 696.5°/day (rotation rate of 1.407×10^{-4} Hz)

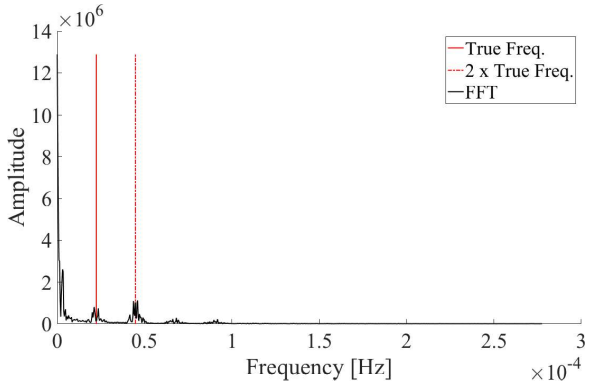

Figure 8. FFT of the light curve in Fig. 7 of Comet 67P

[18], and the true trajectory of the Rosetta spacecraft to simulate these images. The shape model of Comet 67P [17] is shown in Fig. 6(a). First, we generate light curves from these images, as shown in Fig. 7, which is the summation of the brightness intensities of the small body's pixels. Then, we use the Fast-Fourier-Transform (FFT) on these light curves to estimate the rotation rate, as shown in Fig. 8. Note that the peaks of the FFT are at the true frequency and twice the true frequency. The peak at twice the frequency is because of the roughly cylindrical shape of the body that means the maximum area is visible (the intensity peaks) on opposite sides of the body, and hence occurs every half rotation. We use this information to estimate the rotation rate of Comet 67P. The error between the estimated rotation rate and the true rotation rate is shown in Fig. 9. Note that the estimated rotation rate converges to the true rotation rate within 2–3 days.

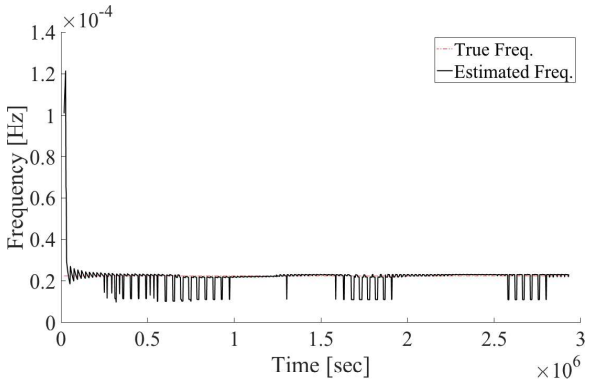

Figure 9. Estimated rotation rate of Comet 67P with respect to time, for the simulated images in Fig. 5

We perform the same analysis for simulated images of Asteroid Itokawa, which has a rotation period of 12.132 hrs (1.437×10^{-4} Hz) [19]. For these simulated images the spacecraft approaches the asteroid along a straight line. The shape model of Asteroid Itokawa [20] is shown in Fig. 6(b). The spacecraft starts 200 km away at t_0 and approaches Asteroid Itokawa at the speed of 5.602 km/day. The simulated images are shown in Fig. 10. The light curve, FFT of the light curve, and error between estimated rotation rate and true rotation rate are shown in Fig. 11, 12, and 13 respectively. The estimated rotation rate converges to the true rotation rate within 2–3 days.

The same process is also performed using real images from the Rosetta mission, as shown in Fig. 15. Note that the

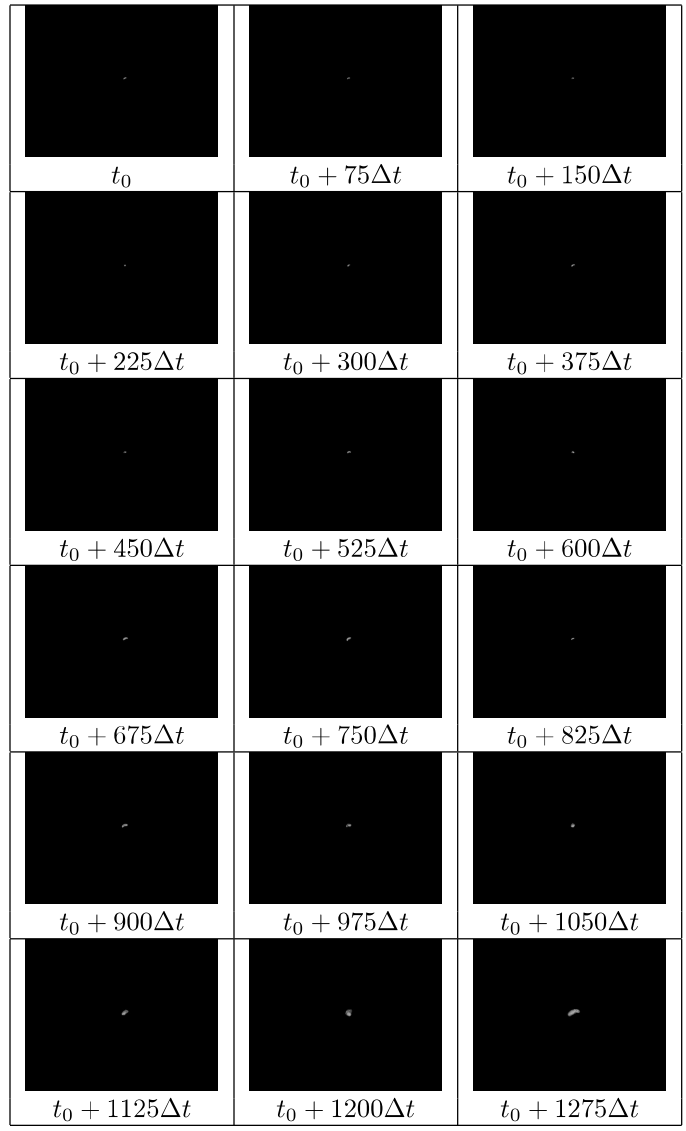

Figure 10. Simulated images of Asteroid Itokawa, where the spacecraft starts 200 km away at t_0 and approaches the asteroid along a straight line at the speed of 5.602 km/day. Here $\Delta t = 30$ mins.

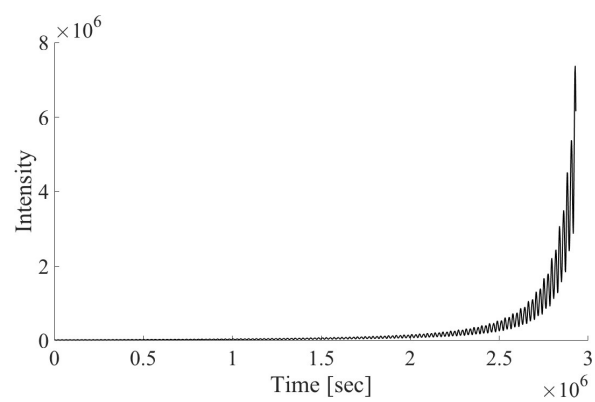

Figure 11. Light curve of Asteroid Itokawa with respect to time, obtained from simulated images in Fig. 10

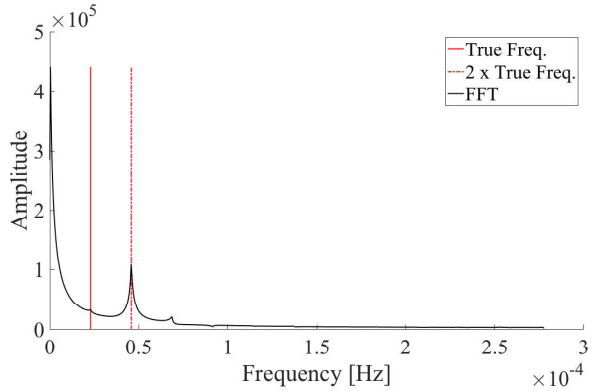

Figure 12. FFT of the light curve in Fig. 11 of Asteroid Itokawa

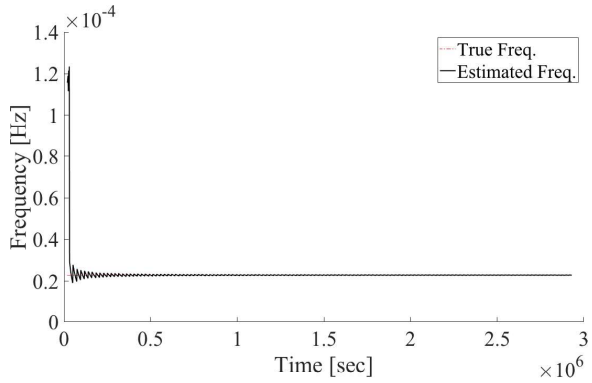

Figure 13. Estimated rotation rate of Asteroid Itokawa with respect to time, of the simulated images in Fig. 10

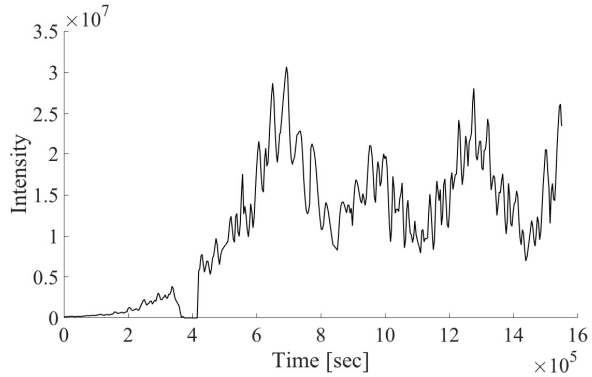

Figure 14. Light curve of Comet 67P with respect to time, obtained from real images in Fig. 15

comet is only partially-visible or not-visible in some of the images because of errors in the Rosetta spacecraft camera pointing angle. The light curve, FFT of the light curve, and error between estimated rotation rate and true rotation rate are shown in Fig. 14 , 16, and 17 respectively. Here, the estimated rotation rate converges to the true rotation rate in ≈ 10 days.

Thus we validated our approach of estimating the rotation rate using both simulated data from 67P and Itokawa, and real data from the Rosetta mission.

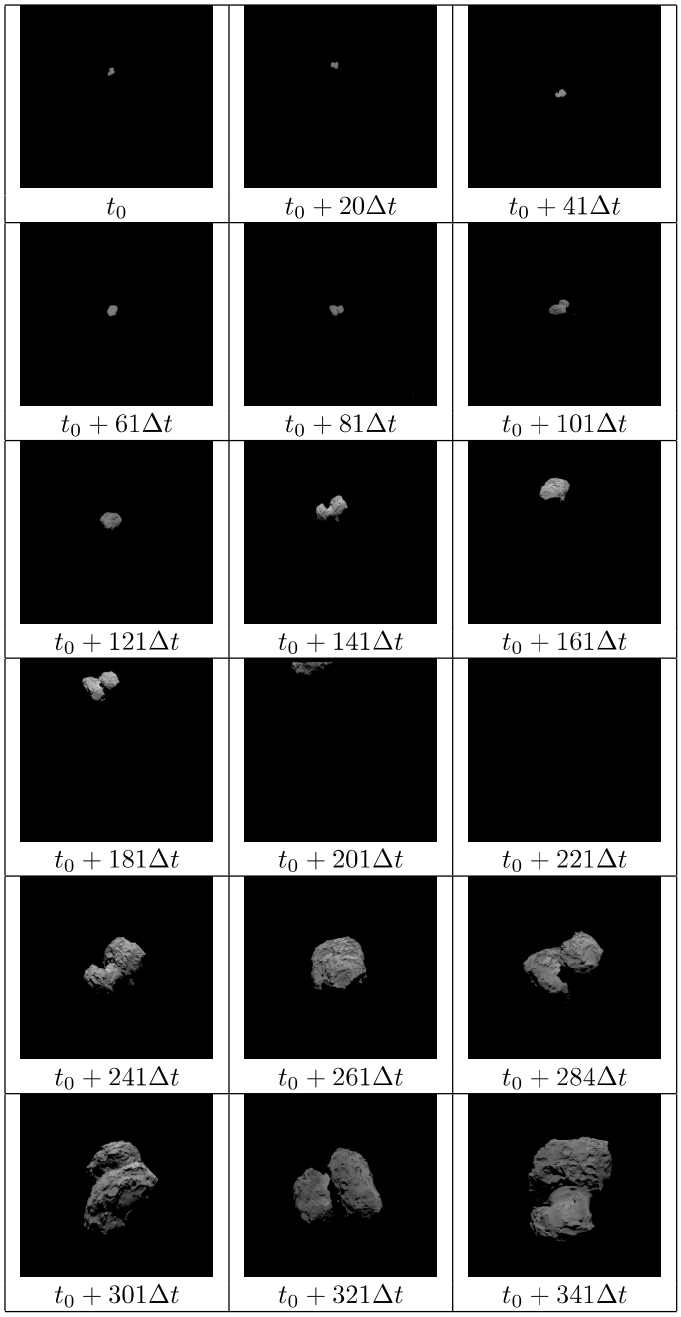

Figure 15. Real images of the Comet 67P from the Rosetta spacecraft. Here $t_0 = 31^{\text{st}}$ July 2014, 10AM and $\Delta t = 30$ mins.

4. Estimating Rotation Center

In this section, we estimate the rotation center of the small body in the images captured by the spacecraft. Even when the small body is only 10s of pixels in the image, its silhouette is in sharp contrast against the dark background as shown in Fig. 18.

Using the rotation period obtained in Section 3 and time-stamp of the images, we match images according to their rotation phase. Since the body can be located anywhere in the image (i.e., the body need not be at the exact center of the field of view of the camera), we need to find the rotation center of the body. In a given image $\mathcal{I}_k$ at k^{th} time instant,

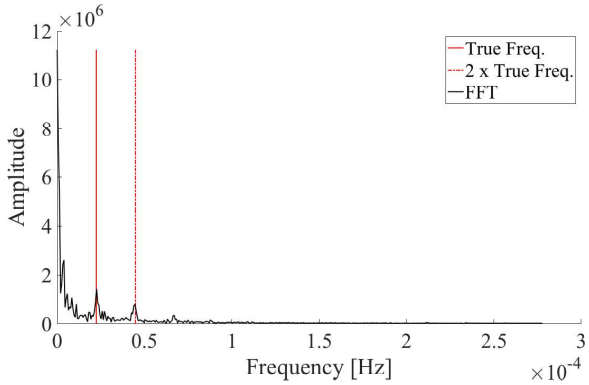

Figure 16. FFT of the light curve in Fig. 14 of Comet 67P

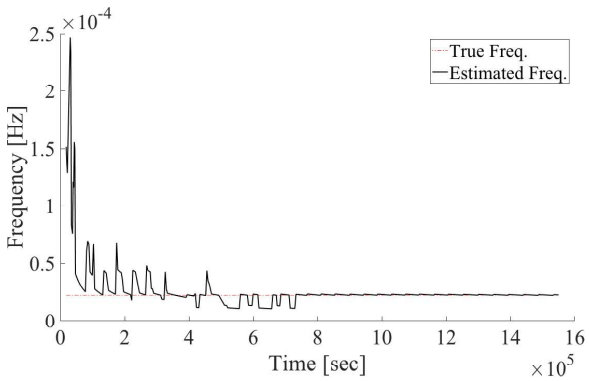

Figure 17. Estimated rotation rate of Comet 67P with respect to time, of the real images in Fig. 15

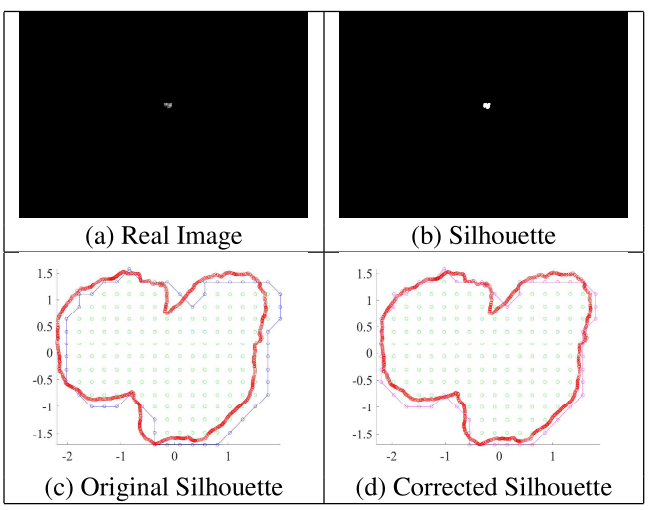

Figure 18. Estimating Rotation Center. For (c) and (d), red dots are the true silhouette. In (c) the blue dots are the observed silhouette centered at the origin. The true center of the silhouette is not at the origin, hence there is an offset. In (d) the pink dots are the observed silhouette with corrections to the estimated center of mass.

let the set $\mathcal{X}_k$ represent all the pixels that form the silhouette of the small body. We make an approximation to estimate the center of mass of the small body as:

$$\text{CM}_{\text{body},k} = \left(\frac{\sum_{(p_x,p_y)\in\mathcal{X}_k} p_x}{|\mathcal{X}_k|}, \frac{\sum_{(p_x,p_y)\in\mathcal{X}_k} p_y}{|\mathcal{X}_k|} \right), \quad (1)$$

where the pixel (p_x, p_y) is at the p_x-row and p_y-column in the image and $|\mathcal{X}_k|$ represents the total number of pixels in $\mathcal{X}_k$. It is empirically observed that images of the opposite phase ($\pm 180°$) are roughly mirror images of the original images, about the rotation axis. Being mirror images, the center offset in the original image should be equal in magnitude and opposite in direction from the mirror image. Therefore, the average of the center of mass of a given the image and the image with the opposite phase is used to estimate the center of rotation of the body.

If the center of mass of the body is predicted to be at the origin, then there can be an offset to the true silhouette, as shown in Fig. 18(c). An estimation of the center can be used to correct the observed silhouette, leading to better alignment with the true silhouette, as shown in Fig. 18(d). This correction of the center is an important step to feed into the Shape from Silhouette algorithm.

5. Estimating 3D Shape using Silhouette-based Reconstruction

A number of algorithms exists in the literature for silhouette-based 3D shape reconstruction using multiple images [21], [22], [23]. These algorithms assume that the position and orientation of the object and the position and orientation of the camera while taking the pictures are precisely known. In our case, we know the rotation rate from Section 3, the center of rotation from Section 4, the distance between the body and the spacecraft, and the orientation of the spacecraft. If we knew the pole of rotation of the body, then we would have enough information to use these existing algorithms. In this section, we assume that we know the pole of rotation, and estimate the 3D shape of the small body. Our algorithm is a slight modification of existing algorithms since we have to account for large changes in distances and errors in the imaging process. In the next Section 6, we will remove this assumption on knowledge of the pole location when we present the complete SfS algorithm.

Our algorithm for silhouette-based 3D shape reconstruction is shown in Algorithm 1.

- First we estimate a bounding box for the small body based on initial estimates of its size. Here we estimate Comet 67P to be inside an $8 \times 8 \times 8$ km cube.
- This bounding box is divided into small cubes or voxels of the desired resolution, where n_V represents the total number of voxels. Our desired resolution is 0.1 km, that results in $\approx 5.3 \times 10^5$ voxels at the start of the process. Let us represent the ith voxel as $\mathcal{V}_i = \{x_i, y_i, z_i, s_i, h_i\}$, where $\{x_i, y_i, z_i\} \in \mathbb{R}^3$ denotes the 3D position of the voxel, $s_i \in \mathbb{R}$ denotes the size of the voxel, and $h_i \in \mathbb{Z}$ denotes the number of hits (explained below) the voxel has received and it is initialized to 0. See line 5.
- Let n_I represents the total number of images and $\mathcal{I}_k$ represent the kth image, where $k \in \{1, \ldots, n_I\}$. The corrected silhouette is computed using the technique shown in Section 4.
- Subsequently, for every image, we project the voxel onto the image plane to check if it is inside the silhouette. If the voxel is outside the silhouette, then it receives a hit. If the number of hits crosses a given threshold T_1, then that voxel is removed. Here, T_1 is empirically determined to be 20. See lines 8–16.
- We also incorporate a forgetting-factor to handle erroneous images or errors in projection. After every pre-determined

Algorithm 1 Silhouette-based 3D Shape Reconstruction

1: Given rotation rate of small body (Section 3)
2: Given distance between the small body and the spacecraft (Assumption 3)
3: Given orientation of the spacecraft (Assumption 4)
4: Given pole of rotation of the small body
5: Given voxels $\mathcal{V}_i$
6: **for** Image $\mathcal{I}_k, \forall k \in \{1, \ldots, n_I\}$ **do**
7: Compute corrected silhouette (Section 4)
8: **for** All Voxel $\mathcal{V}_i$ **do**
9: Project voxel $\mathcal{V}_i$ onto the image plane of $\mathcal{I}_k$
10: **if** Projected voxel is outside the silhouette **then**
11: $\mathcal{V}_i(h_i) = \mathcal{V}_i(h_i) + 1$
12: **end if**
13: **if** $\mathcal{V}_i(h_i) > T_1$ **then**
14: Remove voxel $\mathcal{V}_i$
15: **end if**
16: **end for**
17: **if** $mod(k, T_2) = 0$ **then**
18: **for** All Voxel $\mathcal{V}_i$ **do**
19: **if** $\mathcal{V}_i(h_i) > 0$ **then**
20: $\mathcal{V}_i(h_i) = \mathcal{V}_i(h_i) - 1$
21: **end if**
22: **end for**
23: **end if**
24: **end for**

number of images (T_2), we remove 1 hit from every voxel with non-zero hits. This process helps in retaining voxels that might have got removed if we let the number of errors build up. Here, T_2 is empirically determined to be 10. See lines 17–23.

This process of silhouette-based 3D shape reconstruction is used to generate the shape model of Comet 67P from the simulated images in Fig. 5. Assuming that the pole of rotation (Right Ascension, RA = 66.3°, Declination, Dec = 65.2°) is known, we use Algorithm 1 to reconstruct the shape model in Fig. 19.

In a given image $\mathcal{I}_k$ at k^{th} time instant, the set $\mathcal{X}_k$ represent all the pixels that form the silhouette of the small body. Let $\mathfrak{S}_k$ represent a tight, filled polygon in the image plane, composed of the points in $\mathcal{X}_k$ that have been corrected for the rotation-center offset. Let $\mathfrak{T}_k$ represent a tight, filled polygon that is generated by projecting the true shape model of the small body onto the image plane. Finally, let $\mathfrak{V}_k$ represent a tight, filled polygon that is generated by projecting the estimated 3D shape of the small body at k^{th} time instant onto the image plane. Let $Area(\cdot)$ represent the function to calculate the area of a polygon. We define the following metrics to compute the quality of the 3D shape model being generated, as shown in Fig. 20:

- *Voxel Overlap* measures the area overlap between the true polygon $\mathfrak{T}_k$ and the estimated 3D shape polygon $\mathfrak{V}_k$, normalized against the area of the estimated 3D shape polygon $\mathfrak{V}_k$. This metric starts from a small value, but ends up close to 1 when all the superfluous voxels have been removed.

$$\text{Voxel Overlap} = \frac{Area(\mathfrak{T}_k \cap \mathfrak{V}_k)}{Area(\mathfrak{V}_k)} \,. \tag{2}$$

- *True Overlap* measures the area overlap between the true polygon $\mathfrak{T}_k$ and the estimated 3D shape polygon $\mathfrak{V}_k$, normalized against the area of the true polygon $\mathfrak{T}_k$. This metric should always be close to 1 for a good estimate of the shape model.

$$\text{True Overlap} = \frac{Area(\mathfrak{T}_k \cap \mathfrak{V}_k)}{Area(\mathfrak{T}_k)} \,. \tag{3}$$

Note that neither the voxel overlap nor true overlap metrics can be computed onboard the spacecraft. Therefore, we define the following metric that is similar to the true overlap,

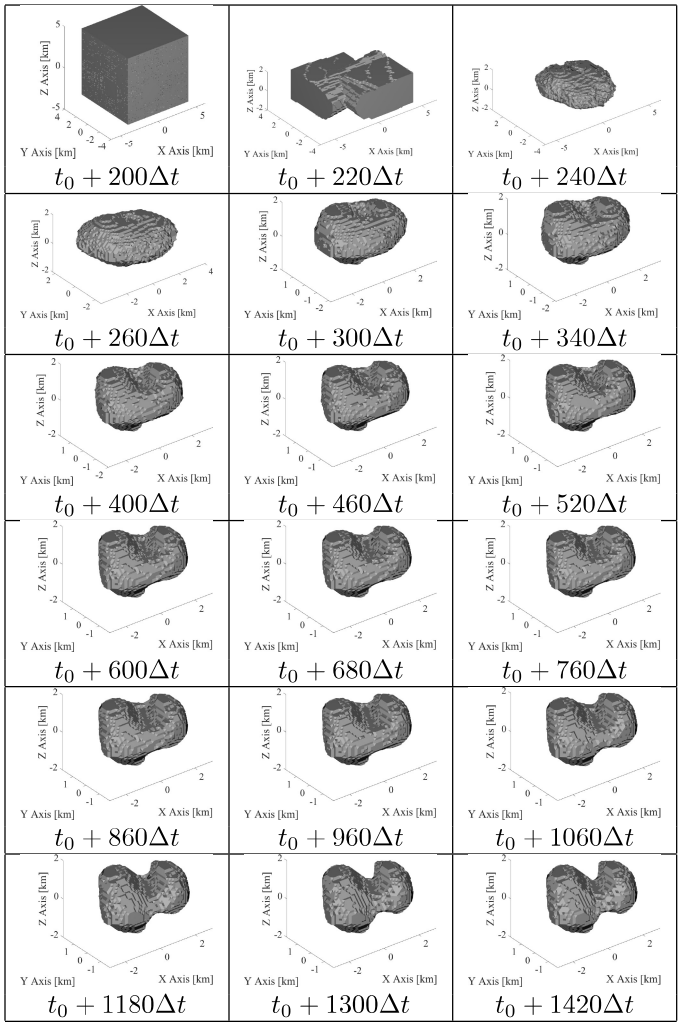

Figure 19. 3D shape of Comet 67P is reconstructed using the simulated images in Fig. 5.

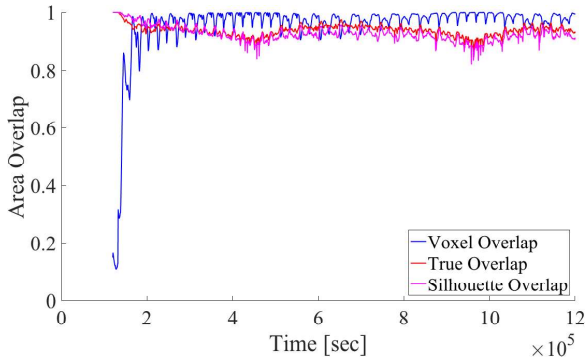

Figure 20. The three metrics to determine quality of the estimated 3D shape

but it can be computed onboard the spacecraft.

• *Silhouette Overlap* measures the area overlap between the silhouette-based polygon $\mathfrak{S}_k$ and the estimated 3D shape polygon $\mathfrak{V}_k$, normalized against the area of the observed silhouette-based polygon $\mathfrak{S}_k$. This metric relies on the fact that the true polygon $\mathfrak{T}_k$ and silhouette-based polygon $\mathfrak{S}_k$ are almost identical, as shown in Fig. 18(d). Like the true overlap metric, this metric should always be close to 1 for a good estimate of the shape model.

$$\text{Silhouette Overlap} = \frac{Area(\mathfrak{S}_k \cap \mathfrak{V}_k)}{Area(\mathfrak{S}_k)}. \tag{4}$$

Since the silhouette overlap metric can be computed onboard the spacecraft, it will be used to assess guesses of the pole of rotation in the SfS Algorithm.

We are now ready to present the complete SfS algorithm in Section 6.

6. Shape from Silhouette (SfS) Algorithm

We know the rotation rate from Section 3 and the center of rotation from Section 4. Assuming the pole of rotation, we can reconstruct the 3D shape using the algorithm in Section 5. In this section, we present the complete SfS algorithm that estimates the pole of rotation while reconstructing the 3D shape of the body. The key insight here is that only the correct pole will give low silhouette overlap errors in Algorithm 1. Therefore, a brute-force search across all possible poles is used to estimate the correct pole.

Algorithm 2 Shape from Silhouette (SfS)

Given rotation rate of small body (Section 3)
Given distance between the small body and the spacecraft (Assumption 3)
Given orientation of the camera in the spacecraft (Assumption 4)
Initialize $P_{\text{best}} = (0°, 0°)$
Execute Algorithm 1 to initialize SO_{best}
while $SO_{\text{best}} < T_3$ **do**
    Estimate next iteration of pole P_{iter}
    Execute Algorithm 1 to compute silhouette overlap value SO_{iter} for this pole
    if $SO_{\text{iter}} > SO_{\text{best}}$ **then**
        $P_{\text{best}} = P_{\text{iter}}$
        $SO_{\text{best}} = SO_{\text{iter}}$
    end if
end while

The SfS algorithm is given in Algorithm 2. Let the variable P_{best} represent the best location of the pole. It is initialized to (RA = 0°, Dec = 0°). Let the variable SO_{best} represent the best silhouette overlap value. The Algorithm 1 is executed using P_{best} to initialize SO_{best}. Let T_3 represent a threshold for acceptable silhouette overlap value. Here we use $T_3 = 0.9$, which was determined empirically. For each iteration of the while loop, a new pole value is estimated, and its corresponding silhouette overlap value is computed using Algorithm 1. This process terminates when a good enough pole is found that satisfies the threshold condition. Then the variable P_{best} gives the best estimate of the pole.

The SfS algorithm is used to estimate the pole and shape of Comet 67P using the simulated images in Fig. 5. The results are shown in Fig. 21. Note that the true pole is at RA = 66.3° and Dec = 65.2°. The resolution of this process is limited to 1° because the apparent size of a voxel (of size $0.1 \times 0.1 \times 0.1$

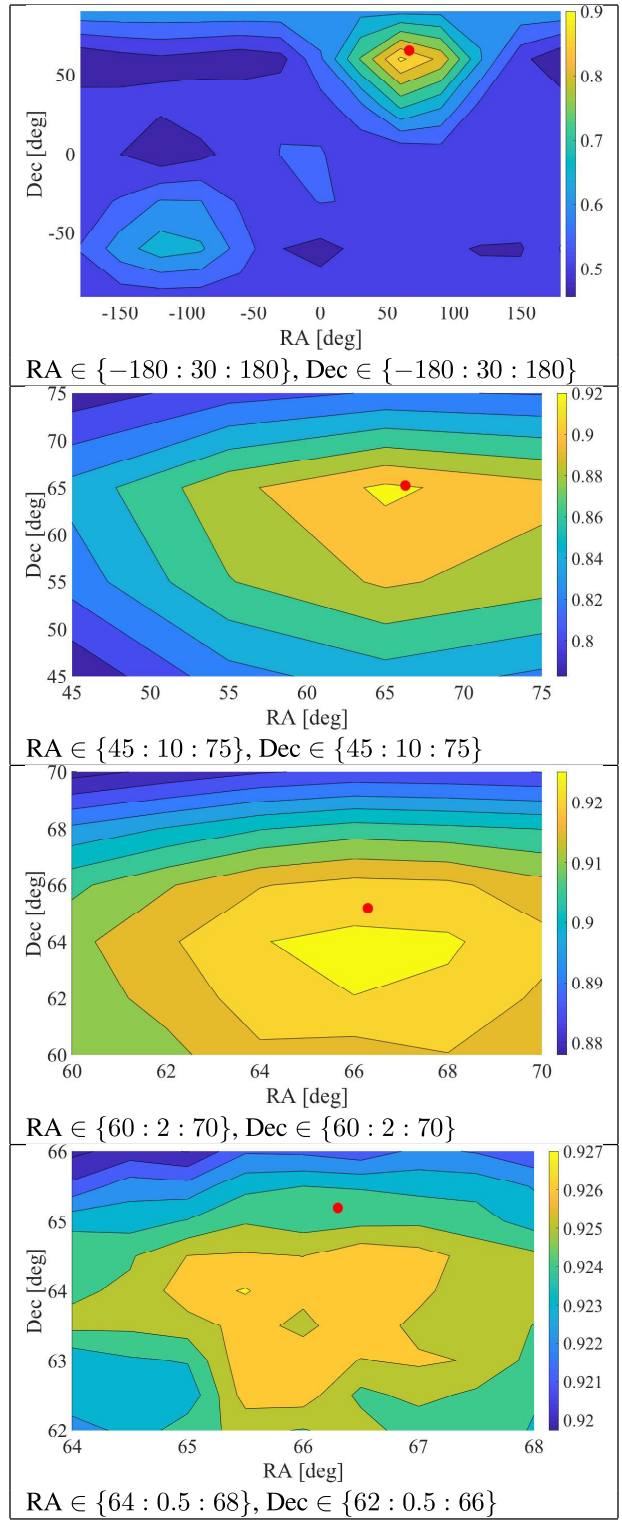

Figure 21. Silhouette overlap values (indicated by the colour scale) for different pole locations for Comet 67P, using the simulated images in Fig. 5. From top to bottom the range of RA and Dec values are focusing on the highest silhouette overlap. The true pole (denoted by ●) is at RA $= 66.3°$ and Dec $= 65.2°$.

km), when viewed from the spacecraft, is $\approx 1°$.

7. Numerical Simulations

We now discuss the robustness to shape models and sensitivity to sun angles of the SfS algorithm in Algorithm 2.

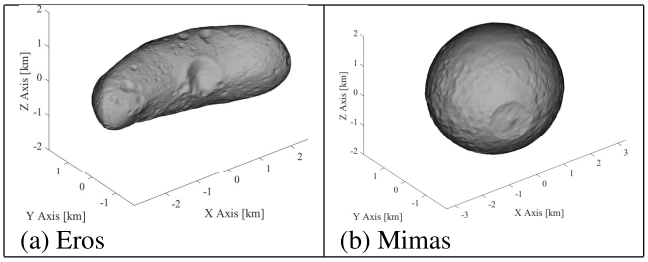

Figure 22. Re-sized shape models of the asteroid 433 Eros and satellite Mimas.

Robustness to Shape Models

In order to test the robustness to shape models, we replace shape model of Comet 67P in the above simulation with the resized shape models of the asteroid 433 Eros [24] and the satellite Mimas [25]. These shape models are shown in Fig. 22.

Since the shape model of Eros is non-spherical, the SfS algorithm estimates its pole at RA $= 66°$ and Dec $= 63.5°$ as shown in Fig. 23, which is within acceptable error bounds from the true pole at RA $= 66.3°$ and Dec $= 65.2°$. The 3D shape reconstructed by the SfS algorithm at the estimated pole location is shown in Fig. 24 and the corresponding area overlap metrics are shown in Fig. 25. These results prove that the estimated 3D shape is of good quality.

However, the SfS algorithm is unable to estimate the pole of the near-spherical satellite Mimas, as shown in Fig. 26, because the silhouette of a spherical object looks similar from all angles. Nonetheless, the estimated pole at RA $= 60°$ and Dec $= 50°$ is within acceptable error bounds from the true pole at RA $= 66.3°$ and Dec $= 65.2°$. The 3D shape reconstructed by the SfS algorithm at the estimated pole location is shown in Fig. 27 and the corresponding area overlap metrics are shown in Fig. 28. These results prove that the estimated 3D shape is of good quality. However there are two peaks in the analysis in Fig. 26 and the second estimate of the pole at RA $= -110°$ and Dec $= -50°$ is almost diametrically opposite to the true pole.

Sensitivity to Sun Angles

We assume perfect illumination in Assumption 2. In order to study the effect of changing sun angles, we vary the sun-angle along three global axes in our simulations. Here $0°$ represents that the sun is directly behind the spacecraft. Here we also assume that the true pole is known. The effect of sun angle on the silhouette overlap metric is shown in Fig. 29. Note that there is a significant reduction in the silhouette overlap metric after $\pm 10°$ sun angle on all three axes. Thus the algorithm is robust only within this range of sun angles.

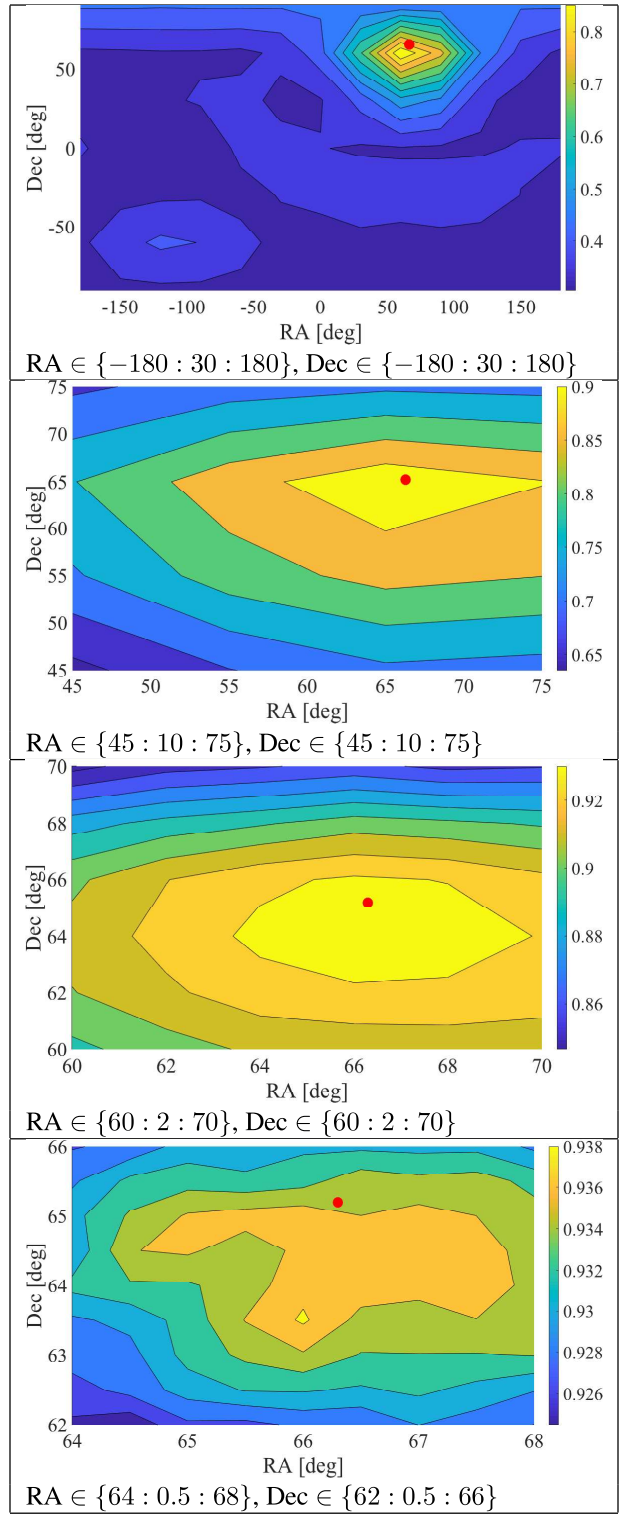

Figure 23. Silhouette overlap values (indicated by the colour scale) for different pole locations for the shape model of Eros. From top to bottom the range of RA and Dec values are focusing on the highest silhouette overlap. The true pole (denoted by ●) is at RA $= 66.3°$ and Dec $= 65.2°$.

8. Conclusion

In this paper, we presented a novel SfS algorithm for reconstructing the 3D shape of small bodies using images where the apparent size of the body is small, by taking advantage of the sharp contrast of the body against its dark background. We estimate the rotation rate using the FFT of the light curve of the small body. Then, using the rotation period and time-stamp of the images, we match images that have the

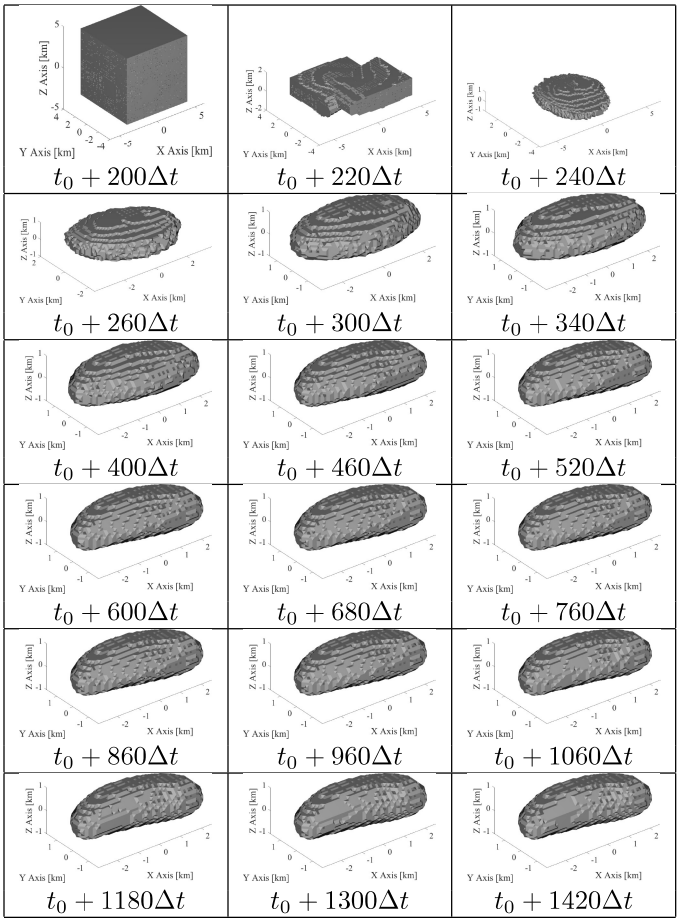

Figure 24. 3D shape of the resized asteroid 433 Eros is reconstructed using simulated images.

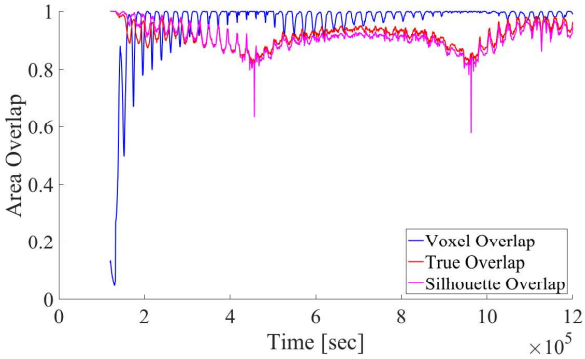

Figure 25. The area overlap metrics show that the estimated 3D shape of the asteroid Eros is good

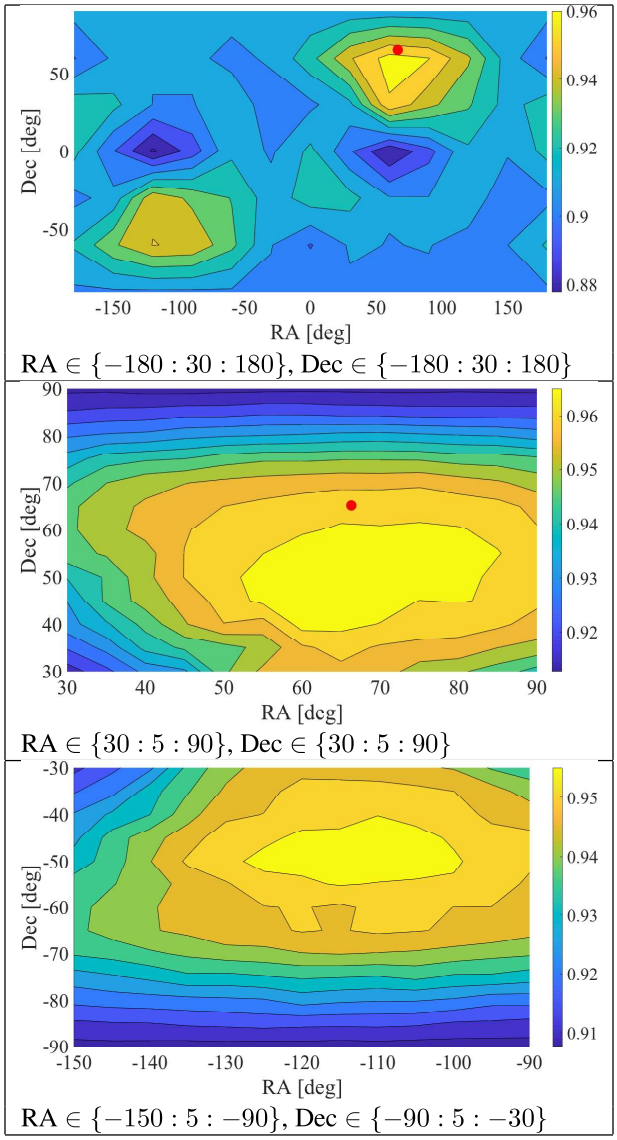

Figure 26. Silhouette overlap values (indicated by the color scale) for different pole locations for the shape model of Mimas. The top image is over the whole range of RA and Dec, and the bottom two each focus on a particular peak. The true pole (denoted by ●) is at RA= 66.3° and Dec= 65.2°.

same rotation phase and estimate the center of rotation of the body. Since the orientation of the rotation axis is unknown, we use multiple hypotheses for the rotation axis to generate corresponding shape models through our SfS algorithm. The model with the highest overlap between the predicted model view and observed silhouette is selected. In this algorithm, we assume that the body has a pure rotation about a principal axis (i.e., not tumbling) and that the Sun is directly behind the spacecraft and fully illuminating the body. The rotation rate algorithm has been tested using simulated data and real data from the Rosetta mission. The SfS algorithm has been tested on simulated data from three small body missions, and has been assessed for sensitivity to sun angles. Future work will test the SfS algorithm on real data and improve the efficiency of the algorithm, with improved shape models and methods for determining the pole. The focus will be to implement the algorithm for tests on data from upcoming missions to asteroids such as Hayabusa-2 or OSIRIS-REx.

ACKNOWLEDGMENTS

This research was carried out at the Jet Propulsion Laboratory, California Institute of Technology, under a contract with the National Aeronautics and Space Administration. ©2018 California Institute of Technology. All rights reserved.

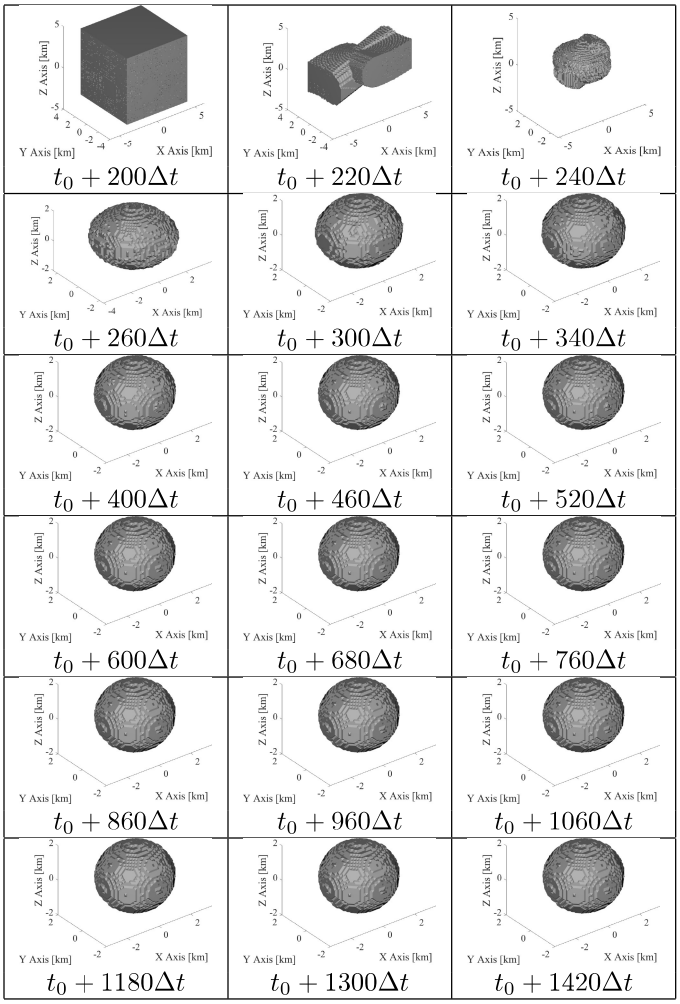

Figure 27. 3D shape of the resized satellite Mimas is reconstructed using simulated images.

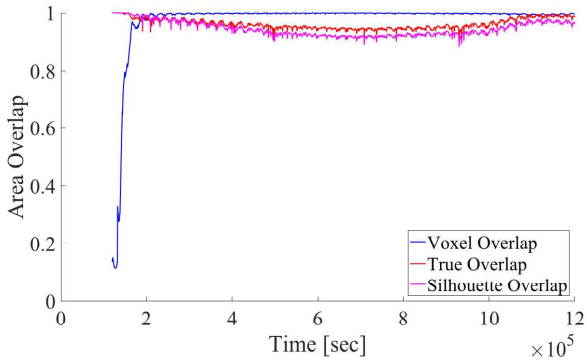

Figure 28. The area overlap metrics show that the estimated 3D shape of the satellite Mimas is good

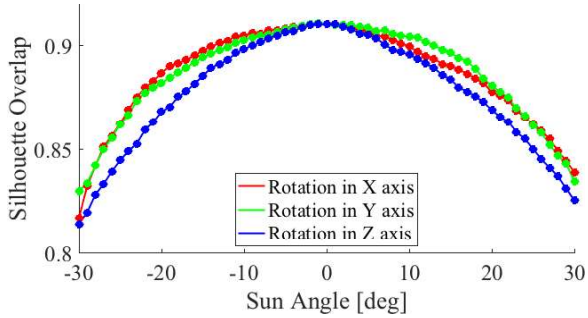

Figure 29. The silhouette overlap metric decreases with increasing sun angle.

References

[1] A. Fujiwara, J. Kawaguchi, D. Yeomans, M. Abe, T. Mukai, T. Okada, J. Saito, H. Yano, M. Yoshikawa, D. Scheeres *et al.*, "The rubble-pile asteroid Itokawa as observed by Hayabusa," *Science*, vol. 312, no. 5778, pp. 1330–1334, 2006.

[2] K.-H. Glassmeier, H. Boehnhardt, D. Koschny, E. Kührt, and I. Richter, "The Rosetta mission: Flying towards the origin of the solar system," *Space Science Reviews*, vol. 128, no. 1-4, pp. 1–21, 2007.

[3] J. Biele, S. Ulamec, E. Jurado, E. Canalias, A. Blazquez, T. Martin, and M. Küppers, "Rosetta comet mission close proximity operations at comet 67P/Churyumov-Gerasimenko and landing Philae," in *Lunar and Planetary Science Conf.*, Woodlands, TX, Mar. 2013.

[4] M. F. AHearn, M. Belton, W. Delamere, J. Kissel, K. Klaasen, L. McFadden, K. Meech, H. Melosh, P. Schultz, J. Sunshine *et al.*, "Deep Impact: excavating comet Tempel 1," *Science*, 2005.

[5] C. T. Russell and C. A. Raymond, "The Dawn mission to Vesta and Ceres," in *The Dawn Mission to Minor Planets 4 Vesta and 1 Ceres*. New York, NY: Springer, 2011, pp. 3–23.

[6] JAXA. Hayabusa. URL: http://planetary.s3.amazonaws.com/assets/images/spacecraft/2018/20180215_hayabusa-at-itokawa.jpg [cited December 11, 2018].

[7] ESA. Rosetta. URL: http://www.esa.int/var/esa/storage/images/esa_multimedia/images/2014/09/rosetta_and_its_target_comet/14772820-1-eng-GB/Rosetta_and_its_target_comet.jpg [cited December 11, 2018].

[8] Jet Propulsion Laboratory, California Institute of Technology. Mission to Comet Tempel 1 Deep Impact. URL: https://www.jpl.nasa.gov/missions/deep-impact/ [cited December 11, 2018].

[9] Y. Tsuda, M. Yoshikawa, M. Abe, H. Minamino, and S. Nakazawa, "System design of the Hayabusa 2 – asteroid sample return mission to 1999 JU3," *Acta Astronautica*, vol. 91, pp. 356–362, 2013.

[10] M. C. Nolan, C. Magri, E. S. Howell, L. A. Benner, J. D. Giorgini, C. W. Hergenrother, R. S. Hudson, D. S. Lauretta, J.-L. Margot, S. J. Ostro *et al.*, "Shape model and surface properties of the OSIRIS-REx target asteroid (101955) Bennu from radar and lightcurve observations," *Icarus*, vol. 226, no. 1, pp. 629–640, 2013.

[11] P. Lord, S. Tilley, D. Y. Oh, D. Goebel, C. Polanskey, S. Snyder, G. Carr, S. M. Collins, G. Lantoine, D. Landau, and L. Elkins-Tanton, "Psyche: Journey to a metal world," 2017.

[12] H. F. Levison, C. Olkin, K. S. Noll, S. Marchi, and Lucy Team, "Lucy: Surveying the diversity of the trojan asteroids: The fossils of planet formation," 2017.

[13] W. M. Owen Jr, "Methods of optical navigation," Jet

Propulsion Laboratory, National Aeronautics and Space Administration, Pasadena, CA, Tech. Rep., 2011.

[14] R. Gaskell, O. Barnouin-Jha, D. J. Scheeres, A. Konopliv, T. Mukai, S. Abe, J. Saito, M. Ishiguro, T. Kubota, T. Hashimoto *et al.*, "Characterizing and navigating small bodies with imaging data," *Meteoritics & Planetary Science*, vol. 43, no. 6, pp. 1049–1061, 2008.

[15] M. J. Sidi, *Spacecraft Dynamics and Control*. Cambridge, U.K.: Cambridge Univ. Press, 1997.

[16] P. Pravec, A. Harris, D. Vokrouhlickỳ, B. Warner, P. Kušnirák, K. Hornoch, D. Pray, D. Higgins, J. Oey, A. Galád *et al.*, "Spin rate distribution of small asteroids," *Icarus*, vol. 197, no. 2, pp. 497–504, 2008.

[17] ESA. 3D Model of Rosetta's comet 67P C-G. URL: http://open.esa.int/rosetta-3d-model/ [cited December 11, 2018].

[18] S. Mottola, S. Lowry, C. Snodgrass, P. Lamy, I. Toth, A. Rożek, H. Sierks, M. AHearn, F. Angrilli, C. Barbieri *et al.*, "The rotation state of 67p/churyumov-gerasimenko from approach observations with the osiris cameras on rosetta," *Astronomy & Astrophysics*, vol. 569, p. L2, 2014.

[19] J. Ďurech, D. Vokrouhlickỳ, M. Kaasalainen, P. Weissman, S. Lowry, E. Beshore, D. Higgins, Y. N. Krugly, V. Shevchenko, N. Gaftonyuk *et al.*, "New photometric observations of asteroids (1862) Apollo and (25143) Itokawa – an analysis of YORP effect," *Astronomy & Astrophysics*, vol. 488, no. 1, pp. 345–350, 2008.

[20] R. Gaskell, J. Saito, M. Ishiguro, T. Kubota, T. Hashimoto, N. Hirata, S. Abe, O. Barnouin-Jha, and D. Scheeres, "Gaskell itokawa shape model v1. 0," *NASA Planetary Data System*, 2008.

[21] A. Y. Mulayim, U. Yilmaz, and V. Atalay, "Silhouette-based 3-D model reconstruction from multiple images," *IEEE Transactions on Systems, Man, and Cybernetics, Part B (Cybernetics)*, vol. 33, no. 4, pp. 582–591, 2003.

[22] H.-Y. Lin and J.-R. Wu, "3D reconstruction by combining shape from silhouette with stereo," in *Pattern Recognition, 2008. ICPR 2008. 19th International Conference on*. Citeseer, 2008, pp. 1–4.

[23] K.-M. Cheung, S. Baker, and T. Kanade, "Shape-from-silhouette across time part i: Theory and algorithms," *International Journal of Computer Vision*, vol. 62, no. 3, pp. 221–247, 2005.

[24] R. Gaskell, "Gaskell eros shape model v1. 0," *NASA Planetary Data System*, 2008.

[25] ——, "Gaskell mimas shape model v2. 0," *NASA Planetary Data System*, 2013.

BIOGRAPHY

Saptarshi Bandyopadhyay *is currently a Robotics Technologist at the Jet Propulsion Laboratory, California Institute of Technology. He received his Ph.D. in Aerospace Engineering in January 2016 from the University of Illinois at Urbana-Champaign (UIUC). Saptarshi received his Dual Degree (B.Tech and M.Tech) in Aerospace Engineering in 2010 from the Indian Institute of Technology Bombay, India. At IIT Bombay, he co-founded and led the student satellite project. IIT Bombay's Pratham satellite was launched into low Earth orbit in September 2016. Saptarshi won the gold medal for India at the 9th International Astronomy Olympiad held in Ukraine in 2004. Saptarshi's research interests include aerospace systems, robotics, multi-agent systems and swarms, dynamics and controls, estimation theory, probability theory, and systems engineering.*

Issa Nesnas *is a principal technologist and the supervisor of the Robotic Mobility group at the Jet Propulsion Laboratory with over two decades of research in space robotics and industrial automation. He leads research in autonomy and mobility with a focus on extreme terrain access and microgravity mobility. He contributed to the development of autonomous rover navigation and visual target tracking and participated in the development of the Curiosity and Mars 2020 rovers. Dr. Nesnas served on NASAs Capability Leadership Team for Autonomy and was the co-chair for NASAs Technology Roadmaps for Robotics and Autonomous Systems. He holds several patents and has over fifty publications in this field. He holds a B.E. degree in Electrical Engineering from Manhattan College and a M.S. and Ph.D. in Mechanical Engineering with a specialization in robotics from the University of Notre Dame.*

Shyam Bhaskaran *began his professional career at the Jet Propulsion Laboratory in January of 1992 as an orbit determination specialist on the Galileo mission. Since then, he has served as a member and lead of the navigation team for many missions. He is the one of the principal architects of the autonomous navigation system used on the Deep Space 1, STARDUST, and Deep Impact missions. He then moved into management, serving as the Mission Management Office Team Chief for Guidance, Navigation and Control, during which time he oversaw the successful navigation efforts of STARDUST's flyby of the comet Wild 2, the Genesis Earth return, and Deep Impact's encounter with comet Tempel 1. Since 2005, Dr. Bhaskaran has been the Supervisor for the Outer Planet Navigation Group in the Mission Design and Navigation Section. As manager of this group, Dr. Bhaskaran is responsible for the technical and administrative oversight of 15 engineers responsible for navigation analysis and operations of several current and future missions, including Cassini, Dawn, Juno, and Europa Clipper. Dr. Bhaskaran's honors include two NASA Exceptional Achievement Medals, awards for Technical Excellence, and a NASA Space Act Award for his work on the Deep Space 1 Autonomous Navigation System. He has*

also received over 20 NASA Group Achievement Awards for his work on the various missions listed above. Dr. Bhaskaran received a B.S (1985). and M.S. (1987) from the University of Texas at Austin, and a Ph.D (1991) from the University of Colorado at Boulder, all in Aerospace Engineering.

Benjamin Hockman *is a Robotics Technologist at the NASA Jet Propulsion Laboratory, California Institute of Technology. He received is PhD in Mechanical Engineering from Stanford University in June 2018, where his thesis work focused on the design, control, and autonomy for the robotic exploration of small solar system bodies, such as asteroids and comets. Ben received his Bachelors in Mechanical and Aerospace Engineering from the University of Delaware in 2013. He was a recipient of an NSF Graduate Research Fellowship and several best paper and presentation awards. Ben's research interests span robotic locomotion, estimation, planning and decision making in extreme environments. Specifically, he has worked in planning and decision making for highly stochastic systems, mobility architectures for microgravity and extreme terrain, dynamic grasping of free floating objects, and localization in sensor-deprived environments.*

Benjamin Morrell *is a Postdoctoral Researcher at the NASA Jet Propulsion Laboratory, California Institute of Technology. He is under examination for his PhD at the University of Sydney in the School of Aerospace Mechanical and Mechatronic Engineering. Benjamin completed his Bachelors of Aeronautical (Space) Engineering at the University of Sydney in 2013. In 2015, he was fortunate enough to receive the Australia to US, American Australian Association Fellowship to support a year of study at Texas A&M University. His research focus is on autonomous navigation systems, in particular on visual localization, mapping, trajectory planning and control, for flying robots on Earth and in space.*